The Astrophysical Journal, 700:L118–L122, 2009 August 1 doi:10.1088/0004-637X/700/2/L118

COLLISIONAL STRIPPING AND DISRUPTION OF SUPER-EARTHS

Robert A. Marcus[1], Sarah T. Stewart[2], Dimitar Sasselov[1], and Lars Hernquist[1]
[1] Astronomy Department, Harvard University, Cambridge, MA 02138, USA
[2] Department of Earth and Planetary Sciences, Harvard University, Cambridge, MA 02138, USA
Received 2009 May 15; accepted 2009 June 23; published 2009 July 13

ABSTRACT

The final stage of planet formation is dominated by collisions between planetary embryos. The dynamics of this stage determine the orbital configuration and the mass and composition of planets in the system. In the solar system, late giant impacts have been proposed for Mercury, Earth, Mars, and Pluto. In the case of Mercury, this giant impact may have significantly altered the bulk composition of the planet. Here we present the results of smoothed particle hydrodynamics simulations of high-velocity (up to $\sim 5 v_{\rm esc}$) collisions between 1 and 10 $M_\oplus$ planets of initially terrestrial composition to investigate the end stages of formation of extrasolar super-Earths. As found in previous simulations of collisions between smaller bodies, when collision energies exceed simple merging, giant impacts are divided into two regimes: (1) disruption and (2) hit-and-run (a grazing inelastic collision and projectile escape). Disruption occurs when the impact parameter is near zero, when the projectile mass is small compared to the target, or at extremely high velocities. In the disruption regime, we derive the criteria for catastrophic disruption (when half the total colliding mass is lost), the transition energy between accretion and erosion, and a scaling law for the change in bulk composition (iron-to-silicate ratio) resulting from collisional stripping of a mantle.

Key words: planetary systems: formation – planets and satellites: formation

1. INTRODUCTION

To date, more than 300 extrasolar planets have been discovered. Of these, more than 10 have masses $\lesssim 10\,M_\oplus$. With the launch of the COROT (Bordé et al. 2003) and Kepler (Borucki et al. 2003) satellites, it is expected that many transiting super-Earths will be discovered in the next few years. In fact, the first transiting super-Earth candidate, CoRoT-7b, has been announced (A. Leger et al. 2009, in preparation). The radius determined from the transit, when combined with radial velocity measurements of the planet's mass, can be used to determine a mean density and thus infer a bulk composition (Valencia et al. 2007).

Although the chemical composition of planets in the solar system generally reflects the gradient in the nebula, the final collisions forming each planet may involve embryos scattered from regions with different bulk composition; hence the final composition of each planet is thought to be dominated by the last few impact events (e.g., Wetherill 1994; Chambers 2004). Planet formation simulations have found that late stage impacts can reach velocities up to six times the mutual escape velocity in the terrestrial planet region of the solar system (Agnor et al. 1999). Due to the presence of giant planets and planetary migration, impact velocities may be even higher in other planetary systems (e.g., Raymond et al. 2005b; Mandell et al. 2007). Thus, the formation of super-Earths may involve very high velocity impacts between large bodies (e.g., 0.1 to several Earth masses). Collision outcomes will vary widely depending on the impact velocity, mass ratio between the bodies, and the impact angle (Agnor & Asphaug 2004; Asphaug 2009; Stewart & Leinhardt 2009). The conditions for imperfect merging are particularly interesting as they provide an opportunity to further alter the bulk compositions of the growing planets. An erosive impact event may be responsible for the high bulk density of Mercury relative to the other terrestrial planets in the solar system (Benz et al. 1988, 2007). In addition, collisional erosion has been considered for the Earth–Moon impact (O'Neill & Palme 2008).

The end stages of planet formation are typically studied using *N*-body codes that assume perfect merging of the masses of colliding embryos (e.g., Agnor et al. 1999; Chambers 2009). However, Agnor et al. (1999) showed that the assumption of perfect merging often leads to the combined body rotating faster than the critical limit. Recently, various hybrid techniques combine *N*-body dynamics and a statistical treatment of fragmentation (e.g., Charnoz & Morbidelli 2003; Bromley & Kenyon 2006). The adopted fragmentation models are usually derived from simulations of erosive collisions over a range of target sizes and impact velocities (e.g., Benz & Asphaug 1999; Benz 2000; Stewart & Leinhardt 2009). Models of planetary accretion (still assuming perfect merging) now encompass the formation of extrasolar systems with super-Earths and giant planets (e.g., Thommes et al. 2008). Hence, there is a need for simple descriptions of the outcome of collisions between large planetary embryos.

To complicate matters, recent studies of collisions between planetary embryos describe two dramatically different regimes when the impact energies exceed perfect merging (Agnor & Asphaug 2004; Asphaug et al. 2006; Asphaug 2009): (1) erosion via disruption and gravitational dispersal and (2) "hit-and-run" events where the projectile grazes the target, which is left nearly intact. The boundary between the two regimes depends on the mass ratio and impact angle (see Figure 17 in Asphaug 2009). The disruption regime is typically characterized by the catastrophic disruption criteria, Q^*, which is a size-dependent curve describing the projectile kinetic energy divided by the target mass such that half the target mass remains. For small bodies ($\lesssim$1 km in diameter), tensile strength, which decreases with size, determines the outcome. For larger bodies, gravity dominates and the largest remnant includes reaccumulated material (Melosh & Ryan 1997). The transition between accretion (net growth of the target) and erosion is determined by the dependence of the mass of the largest remnant on the impact energy. Benz & Asphaug (1999) simulated colliding rocky and icy bodies to determine the catastrophic disruption criteria from scales of centimeters to hundreds of kilometers. They found that the ratio of the largest remnant mass, $M_{\rm lr}$, to the target mass, $M_{\rm targ}$, depends linearly on the impact energy divided by target mass, Q, scaled to Q^*.

This simple relationship has been confounded by the fact that Q^* depends on the target size, impact velocity, mass ratio, and material properties. Thus, previous work relied upon the availability of catastrophic disruption criteria for specific impact scenarios. However, Stewart & Leinhardt (2009) have recently developed a more general expression for the disruption criteria. The ratio $M_{\rm lr}/M_{\rm targ}$ is replaced by $M_{\rm lr}/M_{\rm tot}$, where $M_{\rm tot}$ is the total colliding mass. The impact energy divided by target mass, Q, is replaced by the reduced mass kinetic energy scaled to the total colliding mass, $Q_{\rm R} = \frac{1}{2}\mu V_i^2/M_{\rm tot}$, where μ is the reduced mass and V_i is the impact velocity. Using these variables, the new catastrophic disruption criteria, $Q^*_{\rm RD}$, at which $M_{\rm lr}/M_{\rm tot} = 0.5$ is not dependent on the mass ratio. Additionally, Stewart & Leinhardt (2009) provide parameters that describe a wide range of material properties and impact velocities. However, to date, the catastrophic disruption criteria have not been derived for bodies larger than 100 km.

Here, we simulate a wide range of impacts between planetary embryos up to and including super-Earths to derive the conditions for accretion versus erosion. We consider bodies with initial compositions similar to Earth and derive scaling laws for catastrophic disruption and changes to the iron-to-silicate mass ratio resulting from erosion.

2. METHOD

2.1. Smoothed Particle Hydrodynamics (SPH)

Hydrodynamic codes have been used extensively to simulate giant impacts. Smoothed particle hydrodynamics (SPH) is a Lagrangian technique in which the mass distribution is represented by a finite set of particles evolved with time (Gingold & Monaghan 1977; Lucy 1977). To date, SPH has been used to study giant impacts in the early histories of Earth (Benz et al. 1986; Canup 2004), Mercury (Benz et al. 1988, 2007), Mars (Marinova et al. 2008), and Pluto (Canup 2005). These studies have all utilized an SPH code descended from that of Benz et al. (1986).

Here we present the results of simulations of giant impacts using the SPH code GADGET (Springel 2005), which has been tested and utilized extensively in cosmology and galactic dynamics. In particular, GADGET employs a tree-based scheme for computing the self-gravity of objects (Hernquist & Katz 1989), and, unlike other implementations of SPH, a fully conservative approach for integrating the hydrodynamic equations (Springel & Hernquist 2002) that maintains energy and entropy conservation even when smoothing lengths vary adaptively (Hernquist 1993; O'Shea et al. 2005).

We have modified GADGET to compute thermodynamic quantities by interpolating between elements of tabulated equations of state. The tables were generated using a revised version of the semi-analytic equation of state model ANEOS (Thompson & Lauson 1972; Melosh 2007). We used ANEOS parameters for SiO_2 (Melosh 2007), forsterite, and iron (H. J. Melosh 2008, private communication). The EOS tables were finely gridded to resolve phase boundaries (in a manner similar to Senft & Stewart 2008, Appendix). The modified code was tested with three-dimensional simulations of impacts between plates of identical material at multiple resolutions and shock pressures. The calculated peak pressures agree with the analytic impedance match solution (Melosh 1989, p. 54). We performed two additional tests of the code, which are described below. As in previous studies of giant impacts (e.g., Benz et al. 1986), shear and tensile strength are neglected because gravity is expected to dominate in this size regime.

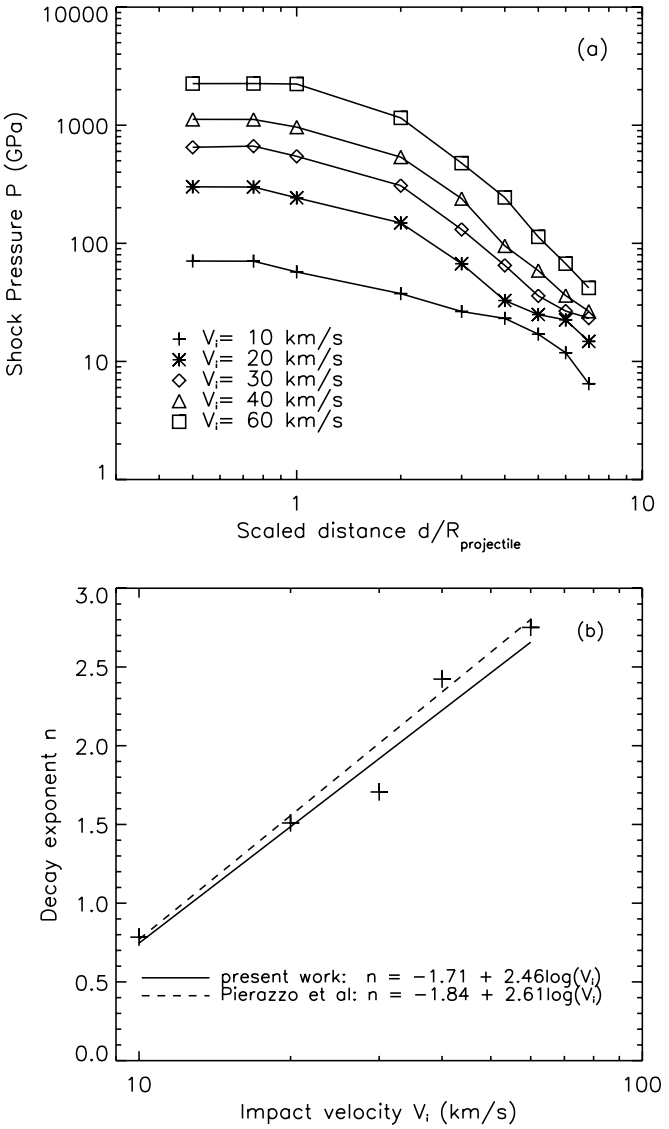

Figure 1. Test One: Shock Pressure Decay. (a) Shock pressure as a function of scaled distance from impact point for an SiO_2 target and projectile. (b) Power-law decay exponent (Equation (1)) as a function of impact velocity, with fits from present work and Pierazzo et al. (1997).

2.2. Test One: Shock Pressure Decay

When a body impacts a half space, beyond an initial isobaric region near the impact point, the peak shock pressure decays exponentially with distance, d, via

$$P \propto d^{-n}, \quad (1)$$

where n is a function of impact velocity. Using a two-dimensional Eulerian hydrocode and a range of materials, Pierazzo et al. (1997) found that $n = (-1.84 \pm 0.17) + (2.61 \pm 0.14)\log(V_i)$, where V_i is the impact velocity in km s^{-1}.

Using our modified version of GADGET, we reproduced the simulations of Pierazzo et al. (1997) for SiO_2 and iron. We modeled the pressure decay profile from a 10 km diameter impactor striking a large flat surface (essentially a half space) at speeds of 10, 20, 30, 40, and 60 km s^{-1}, shown in Figure 1(a). We fit the exponent n with $(-1.70\pm0.33)+(2.45\pm0.24)\log(V_i)$, in excellent agreement with previous work (Figure 1(b)).

Table 1
Test Two: Potential Moon-forming Impacts

$N/10^3$	γ	v	b	M_D/M_L	$L_D/L_{\rm EM}$	$M_{\rm Fe}/M_D$	$M_{\rm imp}/M_D$	$L_F/L_{\rm EM}$	M_M/M_L
					This work				
120	0.13	1.00	0.730	1.40	0.27	0.04	0.78	1.06	1.24
120	0.13	1.00	0.740	1.44	0.30	0.04	0.78	1.07	1.50
					Canup (2004)				
120	0.13	1.00	0.730	1.59	0.30	0.05	0.77	1.16	1.28
120	0.13	1.00	0.740	1.54	0.31	0.04	0.80	1.19	1.44

Notes. N, number of particles; γ, mass ratio; v, impact velocity in units of mutual escape velocity; b, impact parameter; M_D, disk mass; M_L, Lunar mass; L_D, disk angular momentum; $L_{\rm EM}$, angular momentum of Earth–Moon system; $M_{\rm Fe}$, mass of iron in disk; $M_{\rm imp}$, mass of disk originating from impactor; L_F, final system angular momentum; M_M, estimated mass of satellite forming from disk.

2.3. Test Two: Moon-Forming Impact

The iron depletion in the Moon, isotopic similarities between Earth and the Moon, and the large angular momentum of the Earth–Moon system led to the giant impact hypothesis for the origin of the Moon (Hartmann & Davis 1975; Cameron & Ward 1976). SPH has been extensively employed in modeling potential Lunar-forming impacts, most recently by Canup (2004, 2008).

We repeated two of the simulations from Table 1 of Canup (2004). We started from the same initial conditions: a target and impactor of 70% silicates (forsterite) and 30% iron, hydrostatic pressure profile, and an initial isentropic temperature profile with a surface temperature of 2000 K. The target and impactor were allowed to settle to negligible particle velocities in isolation. The final mass of the proto-Earth and proto-Lunar disk were calculated using the iterative procedure described in the Appendix of Canup et al. (2001). Table 1 presents our results from these two simulations, which are in excellent agreement with those of Canup (2004).

2.4. Present Work

We performed a series of more than 60 simulations of impacts onto super-Earth-sized bodies. The initial conditions were targets and impactors of roughly terrestrial composition, comprised of 67% forsterite and 33% iron. The bodies were initialized with hydrostatic pressure profiles and temperature profiles calculated for super-Earths with surface temperatures of about 350 K (Valencia et al. 2006, Figure 4). Previous work did not show a strong dependence on initial temperature (Benz et al. 2007). The bodies were allowed to settle to negligible particle velocities in isolation with the temperature fixed. We used three different target masses, 1 $M_\oplus$, 5 $M_\oplus$, and 10 $M_\oplus$, with impactors of 1/4, 1/2, and 3/4 the target mass. All the initial experiments employed an impact parameter of zero, and a subset was repeated with impact angles of 45°. A few cases of undifferentiated, pure forsterite bodies were considered as a more direct comparison to previous work on catastrophic disruption, which has not included differentiated bodies. The number of particles ranged from 1.25×10^5 to 7×10^5 (30–45 particles per target diameter), and the results were checked for sensitivity to resolution.

The mass of the largest remnant following each impact was determined using a fragment search algorithm similar to that employed by Benz & Asphaug (1999). The potential and kinetic energies of all particles were calculated with respect to the particle closest to the potential minimum. The center of mass position and velocity were then calculated for all bound particles and the process was repeated on the remaining unbound particles until the calculation converged (typically after four or five iterations).

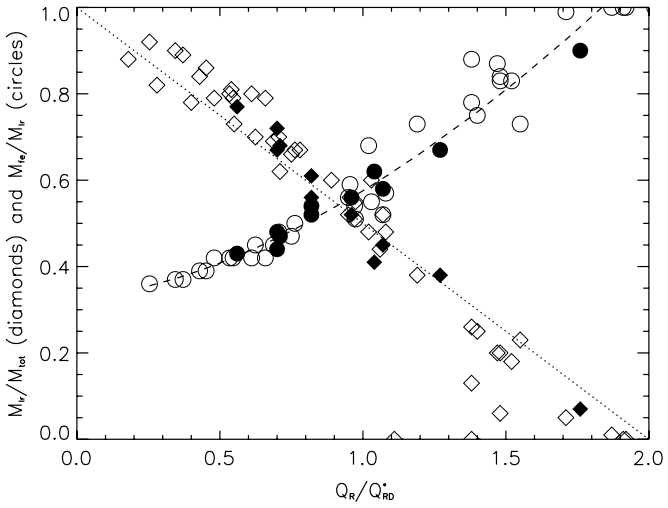

Figure 2. Largest remnant mass and iron fraction vs. scaled impact energy. Open symbols, this work; filled symbols, Benz et al. (1988, 2007). Dotted line, Equation (2); dashed curve, Equation (3).

3. RESULTS

Our results fall into two regimes: (1) disruptive events and (2) hit-and-run events. At impact energies just above merging for events with projectile-to-target mass ratios ranging from 1/10 to 1, the results from Asphaug (2009) indicate that the onset of hit-and-run events occurs at impact angles between 30° and 45° (where 0° is head-on). Our results are in agreement and all the 45° impact cases were merging or hit-and-run events.

3.1. Catastrophic Disruption: Scaling Largest Remnant and Iron Composition

In the disruption regime, the outcome of a collision is described in terms of the largest remnant mass and the catastrophic disruption criteria. In Figure 2, we present the largest remnant mass as a function of the scaled impact energy (diamonds) for our head-on impact events (open symbols) and a subset of simulations from candidate Mercury-forming impacts from Benz et al. (1988, 2007) (filled symbols). The results are in excellent agreement with the universal law for the largest remnant mass presented by Stewart & Leinhardt (2009) (dotted line), where

$$M_{\rm lr}/M_{\rm tot} = -0.5(Q_{\rm R}/Q^*_{\rm RD} - 1) + 0.5. \quad (2)$$

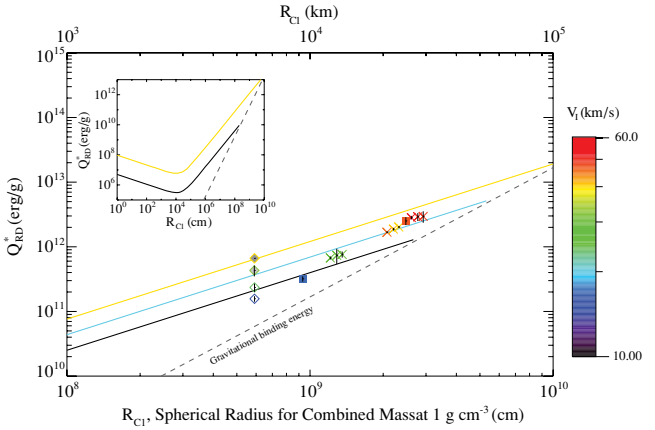

Figure 3. Catastrophic disruption criteria $Q^*_{\rm RD}$ vs. RC_1. Results from impacts between differentiated bodies (×) and pure forsterite bodies (squares). Diamonds are Mercury-size events from Benz et al. (1988, 2007) where shading indicates 0°, 30°, and 45° impacts. Symbol colors indicate impact velocity. Vertical black bars are 1σ errors on $Q^*_{\rm RD}$. Solid lines are disruption criteria for impact velocities of 10 (black), 20 (blue), and 40 km s^{-1} (orange) (Equation (4)). The inset shows full size range for the velocity-dependent catastrophic disruption curves from Stewart & Leinhardt (2009).

This linear relationship derived by Stewart & Leinhardt (2009) for smaller bodies and slower impact velocities continues to hold into the super-Earth regime. Note that the utility of Equation (2) is bounded by $Q_{\rm R}/Q^*_{\rm RD}$ of 0 (events near merging) and 2 (a super-catastrophic regime).

We find that the iron mass fraction of the largest remnant follows a simple power law (circles in Figure 2), given by

$$M_{\rm Fe}/M_{\rm lr} = 0.33 + 0.25(Q_{\rm R}/Q^*_{\rm RD})^{1.65}. \quad (3)$$

Note that we included only the subset of simulations from Benz from which the catastrophic disruption criteria could be derived.

The fitted catastrophic disruption criteria from our simulations and the subset from Benz et al. (1988, 2007) are shown in Figure 3. The lines are the gravity-regime velocity-dependent catastrophic disruption criteria for low-strength bodies from Stewart & Leinhardt (2009) (in cgs units):

$$Q^*_{\rm RD} = 10^{-4} R_{C1}^{1.2} V_i^{0.8}. \quad (4)$$

R_{C1} is the radius of a spherical body with $M_{\rm tot}$ and density of 1 g cm^{-3}. The $Q^*_{\rm RD}$ data points for giant impacts fall short of the prediction from Equation (4) by less than a factor of 2. Hence, the results for super-Earths are entirely consistent with disruption criteria developed for smaller bodies in the gravity regime, and one can reasonably determine the largest remnant mass and bulk composition following a collision knowing only the total colliding mass and impact velocity.

3.2. Disruption Versus Hit-and-Run Impacts

Our high-velocity impacts at angles of 45° by projectile masses between 1/4 and 3/4 the target mass produced no significant change to the mass or the bulk composition of the target. In such cases, there was only an inelastic collision resulting in the target heating and acquiring angular momentum. Hence, we independently verify the phenomenon described as hit-and-run by Asphaug et al. (2006).

The contrast between the disruption and hit-and-run regimes is illustrated by the accretion efficiency defined by Asphaug (2009),

$$\xi \equiv \frac{M_{\rm lr} - M_{\rm targ}}{M_{\rm proj}}, \quad (5)$$

where positive values correspond to growth and negative values to erosion of the target. Note that the value of ξ that corresponds to catastrophic disruption depends on the projectile-to-target mass ratio ($-0.5\, M_{\rm targ}/M_{\rm proj} + 0.5$). Figure 4 presents accretion efficiency as a function of impact velocity, scaled to the mutual escape velocity ($v^2_{\rm esc} = 2G(M_{\rm targ} + M_{\rm proj})/(R_{\rm targ} + R_{\rm proj})$). For head-on impacts (filled black symbols), the fraction of the colliding mass remaining in the largest remnant decreases steadily with increasing $v_i/v_{\rm esc}$. However, for 45° impacts (open symbols), the outcome is nearly a step function from perfect merging to remnant masses approximately equal to the target mass ($\xi = 0$). Our results for super-Earths are in excellent agreement with the studies of accretion efficiency for impacts onto much smaller bodies ($0.10\, M_\oplus$) presented in Agnor & Asphaug (2004) and Asphaug (2009) (e.g., dotted line in Figure 4(a)). Note that the hit-and-run regime encompasses a very large range of impact velocities. In this work, we considered events exceeding $5v_{\rm esc}$, about twice as fast as in previous work. Hence, the possible outcomes of impacts between comparably sized bodies are similar over orders of magnitude in target mass.

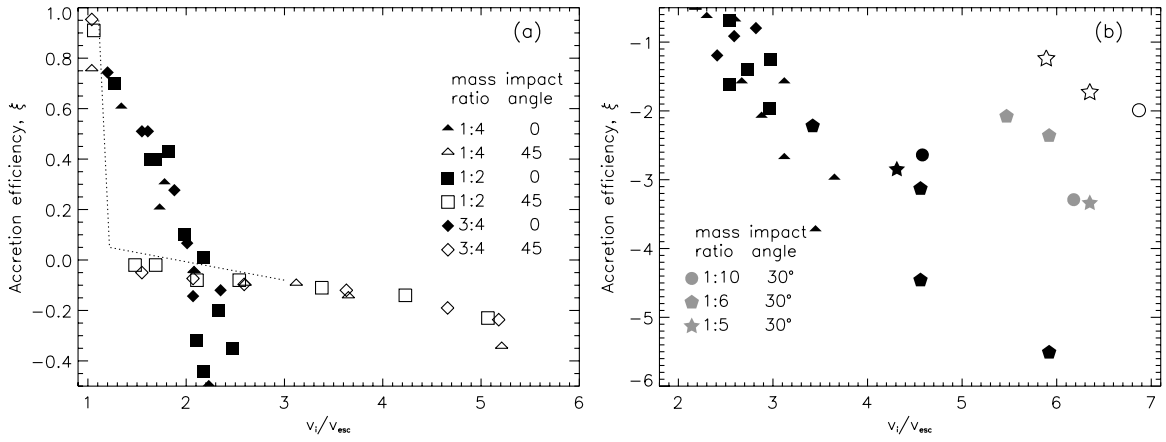

Figure 4. Accretion efficiency, ξ, as a function of scaled impact velocity. (a) Accretion regime. Collision outcome depends strongly on impact angle. Dashed line presents results for 45°, 1:2 mass ratio impacts from Asphaug (2009, Figure 17). (b) Disruption regime. Catastrophic disruption is $\xi = -4.5$, -2.0, and -0.5 for 1:10, 1:5, and 1:2 mass ratios, respectively. In both panels, symbols denote mass ratio and shading denotes impact angle. Circles, pentagons, stars—from Benz et al. (1988, 2007). Other symbols—this work.

At sufficiently high impact energies, the hit-and-run regime transitions to disruption. A study of collisions onto 100 km diameter bodies by projectile masses up to a ratio of 1:10 found that the impact energies required for catastrophic disruption may increase by an order of magnitude or more with increasing impact angle (Figure 1 in Durda et al. 2007). The impact angle dependence is seen in Figure 4(b): near the catastrophic disruption value of $\xi = -2$ for 1:5 mass ratio (stars), compare the offset in velocity for impact angles of 0°, 30°, and 45°. The increased disruption energy as a function of impact angle is given in the diamond points in Figure 3.

Thus, the results of giant impact events at velocities up to several times v_{esc} depend primarily on (1) the impact angle and mass ratio which define the transition between the disruption and hit-and-run regimes and (2) the total colliding mass and impact velocity which define Q^*_{RD} in the disruption regime. The outcome falls in the disruption regime at any impact angle when the projectile is very small and fast but only when the impact angle is small (typically $\lesssim$30°) when the projectile and target are comparably sized. Because 45° is the most probable impact angle, catastrophic disruption of protoplanets is most likely to occur when the impactor is much smaller than the target.

4. DISCUSSION AND CONCLUSIONS

Using the results from this work and previous studies of giant impacts, we have described the outcome of collisions between a wide range of masses, from planetary embryos to super-Earths. In the disruptive regime, the framework developed by Stewart & Leinhardt (2009) to describe the transition between accretion versus erosion in hypervelocity impacts holds from the lab scale, with sizes in centimeters and velocities in m s^{-1}, up to the scales of the largest expected super-Earths, with sizes up to ten thousand kilometers.

In the disruption regime, we derived a scaling law for the changes in bulk composition resulting from collisions between differentiated bodies of Earth-like composition. Based on the boundary between disruptive and hit-and-run type events, significant compositional changes require either a small impact angle or a small, fast projectile. Because of this narrow range of impact conditions that can lead to an increase in bulk density, the presence of unusually dense planets can place constraints on the dynamical history of a planetary system. In particular, if planet growth occurs by merging similar-sized bodies, changes to the bulk composition of the target are unlikely. Thus, one-time high-energy impacts provide the best means of increasing a planet's bulk density. If the specifics of the planetary system rule out such a collision, then such a planet is more likely to have formed in a protoplanetary disk with substantially different chemical abundances or with a density profile quite different from the minimum-mass solar nebula (Raymond et al. 2005a).

For very energetic impacts, the largest remnant can have a substantially different composition than that of Earth, even when the target and impactor initially had Earth-like bulk compositions. This is consistent with the hypothesis that Mercury, which is ∼70% iron by mass, owes its present bulk composition to a catastrophic impact event. For planet masses close to that of Mercury, the critical velocity needed to yield a remnant with such an iron enrichment is about 10–20 km s^{-1}, as was found by Benz et al. (1988, 2007). Such velocities are smaller than the orbital velocities inside 1 AU for a $\sim$1 $M_\odot$ star. However, for more massive planets, the critical velocities can enter the 50–60 km s^{-1} range, requiring extreme conditions for a Mercury-like planet to be created. Thus, Mercury-like planets should be much more common than super-Mercuries, although even these may form in very close orbits in extrasolar systems. Hence, the probability of forming super-Mercuries warrants further investigation (R. A. Marcus et al. 2009, in preparation).

We thank Joe Barranco for help in code development and Zoe Leinhardt, T. J. Cox, and the anonymous reviewer for useful feedback. The simulations in this Letter were run on the Harvard FAS Odyssey cluster.

REFERENCES

Agnor, C., & Asphaug, E. 2004, ApJ, 613, L157
Agnor, C. B., Canup, R. M., & Levison, H. F. 1999, Icarus, 142, 219
Asphaug, E. 2009, Annu. Rev. Earth Planet. Sci., 37, 413
Asphaug, E., Agnor, C. B., & Williams, Q. 2006, Nature, 439, 155
Benz, W. 2000, Space Sci. Rev., 92, 279
Benz, W., Anic, A., Horner, J., & Whitby, J. A. 2007, Space Sci. Rev., 132, 189
Benz, W., & Asphaug, E. 1999, Icarus, 142, 5
Benz, W., Slattery, W. L., & Cameron, A. G. W. 1986, Icarus, 66, 515
Benz, W., Slattery, W. L., & Cameron, A. G. W. 1988, Icarus, 74, 516
Bordé, P., Rouan, D., & Léger, A. 2003, A&A, 405, 1137
Borucki, W. J., et al. 2003, in ESA SP-539, Earths: DARWIN/TPF and the Search for Extrasolar Terrestrial Planets, ed. M. Fridlund, T. Henning, & H. Lacoste (Noordwijk, The Netherlands: ESA), 69
Bromley, B. C., & Kenyon, S. J. 2006, AJ, 131, 2737
Cameron, A. G. W., & Ward, W. R. 1976, Abstracts of the Lunar and Planetary Institute Science Conference, 7, 120
Canup, R. M. 2004, Icarus, 168, 433
Canup, R. M. 2005, Science, 307, 546
Canup, R. M. 2008, Icarus, 196, 518
Canup, R. M., Ward, W. R., & Cameron, A. G. W. 2001, Icarus, 150, 288
Chambers, J. E. 2004, Earth Planet. Sci. Lett., 223, 241
Chambers, J. E. 2009, in Exoplanets, ed. S. Seager, submitted
Charnoz, S., & Morbidelli, A. 2003, Icarus, 166, 141
Durda, D. D., Bottke, W. F., Nesvorný, D., Enke, B. L., Merline, W. J., Asphaug, E., & Richardson, D. C. 2007, Icarus, 186, 498
Gingold, R. A., & Monaghan, J. J. 1977, MNRAS, 181, 375
Hartmann, W. K., & Davis, D. R. 1975, Icarus, 24, 504
Hernquist, L. 1993, ApJ, 404, 717
Hernquist, L., & Katz, N. 1989, ApJS, 70, 419
Lucy, L. B. 1977, AJ, 82, 1013
Mandell, A. M., Raymond, S. N., & Sigurdsson, S. 2007, ApJ, 660, 823
Marinova, M. M., Aharonson, O., & Asphaug, E. 2008, Nature, 453, 1216
Melosh, H. J. 1989, Impact Cratering: A Geologic Process (New York: Oxford Univ. Press)
Melosh, H. J. 2007, Meteorit. Planet. Sci., 42, 2079
Melosh, H. J., & Ryan, E. V. 1997, Icarus, 129, 562
O'Neill, H. S. C., & Palme, H. 2008, R. Soc. Lond. Philos. Trans. A, 366, 4205
O'Shea, B. W., Nagamine, K., Springel, V., Hernquist, L., & Norman, M. L. 2005, ApJS, 160, 1
Pierazzo, E., Vickery, A. M., & Melosh, H. J. 1997, Icarus, 127, 408
Raymond, S. N., Quinn, T., & Lunine, J. I. 2005a, ApJ, 632, 670
Raymond, S. N., Quinn, T., & Lunine, J. I. 2005b, Icarus, 177, 256
Senft, L. E., & Stewart, S. T. 2008, Meteorit. Planet. Sci., 43, 1993
Springel, V. 2005, MNRAS, 364, 1105
Springel, V., & Hernquist, L. 2002, MNRAS, 333, 649
Stewart, S. T., & Leinhardt, Z. M. 2009, ApJ, 691, L133
Thommes, E. W., Matsumura, S., & Rasio, F. A. 2008, Science, 321, 814
Thompson, S. L., & Lauson, H. S. 1972, Tech. Rep. SC-RR-710714 (Sandia Nat. Labs)
Valencia, D., O'Connell, R. J., & Sasselov, D. 2006, Icarus, 181, 545
Valencia, D., Sasselov, D. D., & O'Connell, R. J. 2007, ApJ, 665, 1413
Wetherill, G. W. 1994, Geochim. Cosmochim. Acta, 58, 4513